System and AOCS Challenges for the Design Consolidation of the Next Generation Gravity Mission

System and AOCS Challenges for the Design Consolidation of the Next Generation Gravity Mission

A. Anselmi[1], S. Cesare[2] and S. Dionisio[3]
Thales Alenia Space Italia, Strada Antica di Collegno 253, 10146 Torino (Italy)

C. Novara[4], L. Colangelo [5]
Politecnico di Torino, Torino, 10129, Italy

and

L. Massotti[6] and P. Silvestrin[7]
ESA-ESTEC, Keplerlaan 1, 2201 AZ Noordwijk (The Netherlands)

Since 2003 the European Space Agency (ESA) has promoted studies for the preparation of a "Next Generation Gravity Mission" (provisionally called NGGM) with the objective of measuring the temporal variations of the Earth gravity field over a long time span with unprecedented spatial and temporal resolutions. This mission will have huge impacts on many scientific disciplines based on the study of geophysical phenomena involving the re-distribution and transportation of mass (e.g. geodesy, hydrology, ocean circulation) within the complex Earth system. To accomplish its objectives, the NGGM mission requires a number of innovations, both at technological level and on the control side, if compared to GOCE and GRACE missions. Therefore, it is presented an overview of the latest results of the on-going "Consolidation of the system concept for the Next Generation Gravity Mission" study, carried out by Thales Alenia Space Italia (TAS-I) for the European Space Agency. This paper focuses on the NGGM mission challenges, with a particular care to the relevant system and AOCS technological innovations: the guidance, navigation and control design is provided, in its latest version, for the science phase of the NGGM mission. The model-based control unit is organized in a hierarchical way, where the "drag-free" control plays the role of a wide-band inner loop, and orbit/formation and attitude/pointing controls are narrow band outer loops. The relevant state equations were converted to discrete time providing the embedded model, a part of the control unit: the state predictor, control law, and reference generator were built on and interfaced to the embedded model. Simulated results, via a high-fidelity simulator, prove the concept validity and show that the control performances are in agreement with the mission requirements. Indeed, the control strategy is shown to be capable of keeping the attitude and formation variables stable within the required boundaries, all over the 11-year mission, through a very fine and low thrust authority.

[1] Thales Alenia Space, Strada Antica di Collegno 253, 10146 Torino, Italy, Alberto.Anselmi@thalesaleniaspace.com
[2] Thales Alenia Space, Strada Antica di Collegno 253, 10146 Torino, Italy, Stefano.Cesare@thalesaleniaspace.com
[3] Thales Alenia Space, Strada Antica di Collegno 253, 10146 Torino, Italy, Sabrina.Dionisio@thalesaleniaspace.com
[4] Dipartimento di Elettronica e Telecomunicazioni, Corso Duca degli Abruzzi 24, 10129 Torino, Italy, Carlo.Novara@polito.it
[5] Dipartimento di Automatica e Informatica, Corso Duca degli Abruzzi 24, 10129 Torino, Italy, Luigi.Colangelo@polito.it, AIAA Student Member
[6] Earth Observation Programmes, Future Missions & Instruments Division (ESA-ESTEC EOP-ΦM), Luca.Massotti@ESA.int, AIAA Senior Member.
[7] Earth Observation Programmes, Future Missions & Instruments Division (ESA-ESTEC EOP-Φ), Pierluigi.Silvestrin@ESA.int

I. Introduction

Following the success of GOCE[11] and GRACE[12], the scientific communities and the space agencies have started to focus their attention towards the preparation of a future gravity mission. In particular, since 2003 ESA has promoted studies to establish the scientific requirements, to identify the most appropriate measurement techniques, to start the associated technology developments, and to define the system scenarios for a "Next Generation Gravity Mission" (provisionally called NGGM). The NGGM mission aims at measuring the temporal variations of the Earth gravity field over a long time span (namely a full solar cycle, 11 years) with an unprecedented level of accuracy, both in spatial (comparable to that provided by GOCE) and temporal (weekly or better) resolution.

The last, currently on-going, ESA study for the NGGM mission preparation is the "Consolidation of the system concept for the Next Generation Gravity Mission" study, carried out by Thales Alenia Space in Italy (TAS-I) in 2016-2017 timeframe. The study focuses its activities on the consolidation of the mission concept and of the relevant space segment, with a review of the design of the formation control and of the Attitude and Orbit Control system (AOCS), and the thruster dispatching algorythms. In this paper, highlights on the driving mission and system challenges, togheter with the main technological innovations needed, are illustrated.

II. NGGM Mission Overview

A. Measurement Principle

From the previous studies and from the flight experience of the GRACE and GOCE missions, it turns out that the Low-Low Satellite-to-Satellite Tracking (LL-SST) between satellite pairs flying in loose formation on a low Earth orbit (Figure 1) is the preferred observing technique capable to detect the tiny time-variable gravity signal variations with the required resolution. This technique exploits the satellites themselves as "proof masses" immersed in the Earth gravity field and has an intrinsically higher sensitivity for the geo-potential harmonics of lower degrees and orders than the Satellite Gravity Gradiometry technique (SGG) utilised by GOCE. The fundamental observable is the distance variation between the two satellites centres of mass (COMs) produced by the gravity acceleration, Δd_G, formally obtained as

$$\Delta d_G = \Delta d - \Delta d_D \tag{1}$$

where:

1. Δd is the total distance variation between the COMs, whatever the perturbation source, measured by a distance metrology,
2. Δd_D is the distance variation produced by the non-gravitational (e.g. drag) forces on the satellite COMs along the line joining the COMs themselves:

$$\Delta d_D = \iint \Delta \ddot{d}_D dt^2, \Delta \ddot{d}_D = D_1 - D_2, \tag{2}$$

where $D_1 - D_2$ are the resultant vectors of the non-gravitational accelerations acting on the satellite COMs, measured by the on-board accelerometers.

Therefore, the distance variation between the satellites and their non-gravitational accelerations, measured respectively by a laser interferometer (with nanometric resolution) and by ultra-sensitive accelerometers (of the same class of those embarked on GOCE), are the fundamental scientific observables from which the Earth's gravity field anomalies are retrieved.

B. Scientific Mission Requirements

The products of the NGGM mission will allow investigating with unprecedented detail geophysical phenomena involving re-distribution and transportation of mass in the atmosphere, continental hydrosphere, oceans, cryosphere, and lithosphere, enabling new science in geodesy, geophysics, hydrology, ocean circulation and many other disciplines.

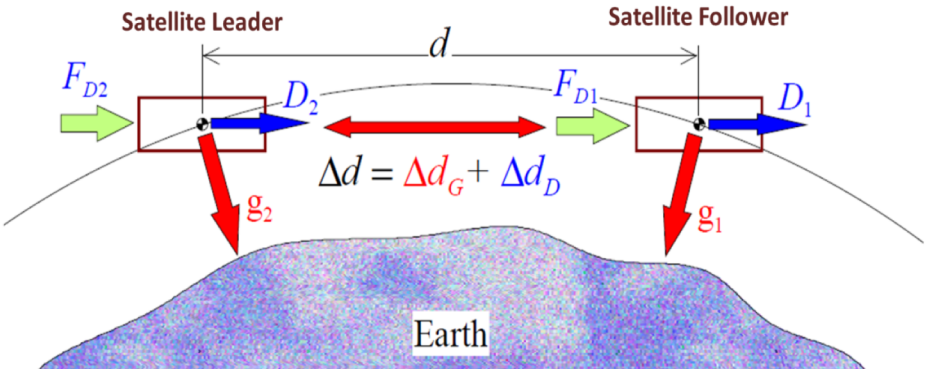

Figure 1. Principle of the LL-SST technique for measuring the Earth's gravity field.

Indeed, mass transport in the Earth's system takes place in several layers located above, at, and below the Earth's surface (concerning Atmosphere, Hydrosphere, Cryosphere and Solid-Earth): the goal of a Next Generation Gravity Mission is to observe the mass transport processes acting in and between these layers. In particular, the Table 1 shows the spatial and temporal scales associated with gravity changes relevant to cryosphere field of prioritization, which should be accomplished by the NGGM. The spatial and temporal scales associated with gravity changes relevant to investigations in hydrology, ocean applications and solid Earth can be found in Ref. 5, togheter with their prioritazion and consolidation in science and user needs.

From the wavelengths of the geo-potential spherical harmonics to be monitored, the spatial measurement

Signal	Time scales	Expected signals: temporal variation in equivalent water height (EWH)	Spatial scale
Changing ice flow dynamics of ice sheets	Long-term	10 m/year 10 cm/year	10 km 500 km
	Monthly to interannual	10 m 10 cm	10 km 500 km
	Daily to weekly	10 m	10 km
Changing SMB of ice sheets	Long-term	2 m/year 20 cm/year	50 km 1000 km
	Seasonal and interannual	2 m 20 cm	50 km 1000 km
	Daily to weekly	1 m 20 cm	10 km 1000 km
Supraglacial, englacial, and subglacial hydrology of ice sheets	Seasonal and interannual	5 m 50 cm	10 km 200 km
	Daily to weekly	10 m	10 km
Glacier mass changes	Long-term	10 m/year 1 m/year	10 km 200 km
	Monthly to interannual	10 m 1 m	10 km 200 km
	Daily to weekly	1 m 10 cm	10 km 50 km
GIA (as a disturbing signal for ice mass balance estimates)	Long-term	5 cm/year 1 cm/year	100 km 1000 km

Table 1. Spatial and temporal scales associated with gravity changes relevant to cryosphere (Ref. 5).

bandwidth (MBW) of the NGGM has been preliminarily established between 1 mHz and 100 mHz (corresponding to a spatial sampling along the orbit between ~77 km and ~7700 km). Furthermore, a polar or near-polar orbit (inclination ≅90°) is deemed necessary in order to avoid gaps around the poles in the geographic coverage, which are undesirable for the study of the ice mass variation in the Arctic and Antarctic regions. The NGGM system study

activities have shown that the requirements in Table 1 can be achieved via a so called Bender constellation with a polar and an inclined pair of satellites (see Figure 2). The design considered in the current system consolidation study accounts for the most challenging satellite pair configuration (inclined one), but it is flexible enough to be accommodated also in a polar orbit.

C. Scientific Control Requirements

To accomplish the scientific objectives, each NGGM satellite shall be designed to undergo minimum disturbances of the payload and shall be endowed with a control system capable of carrying out several tasks in close coordination: orbit maintenance, formation keeping, attitude stabilisation, drag compensation, and laser beam pointing at micro-radian level.

Since the first preparatory ESA studies (Ref. 1-4), the control requirements have been evolved leading to the sub-set summarized in Table 2. Specifically, with respect to the previous NGGM AOCS study, the drag free and satellite pointing requirements have been updated according to the chosen mission orbit, AOCS sensors and actuators. As a result, in Table 2, the main NGGM control functions and the relevant requirements are summarized.

NGGM control requirements		
Control function	**Requirement**	**Remarks**
Orbit altitude	$H = H_{ref} \pm \Delta H$ m For the inclined orbit (inclination of 66°): H_{ref} = 345.3km and ΔH = 100m.	**H** stands for mean orbit altitude **H_{ref}** and **ΔH** depend on the orbit repeat cycle of interest
Satellite formation	SSD = 100 km + 0% ÷ -10%	**SSD** stands for Satellite-to-Satellite Distance. Its value is defined by the metrology's working range and by scientific needs
Non-gravitational accelerations	Lin_acc $\leq 10^{-6}$ m/s^2 Lin_acc_SD $\leq 5 \cdot 10^{-9}$ m/s^2/√Hz in MBW Ang_acc $\leq 10^{-6}$ rad/s^2 Ang_acc_SD $\leq 10^{-8}$ rad/s^2/√Hz in MBW	**Lin_acc/Ang_acc** and **Lin_acc_SD/Ang_acc_SD** stand for the residual linear/angular non-gravitational accelerations in time and relevant Spectral Density. **MBW** stands for Measurement Bandwidth and its range is between 10^{-3} and 10^{-1} Hz.
Satellite pointing	SSL $\leq 2 \cdot 10^{-5}$ rad SSL_SD: $\leq 10^{-5}$ rad/√Hz, for $10^{-3} \leq f < 10^{-2}$ Hz $\leq 2 \cdot 10^{-6}$ rad/√Hz, for $10^{-2} \leq f \leq 10^{-1}$ Hz	**SSL/SSL_SD** stands for satellite pointing along the Satellite-to-Satellite Line and relevant pointing stability in terms of Spectral Density.

Table 2. NGGM control requirements.

III. Satellite Formations and Operational Orbits

In the previous NGGM ESA's studies (Ref. 1-4) several options in terms of orbit altitude and inclination, formation geometry, number of satellite pairs, range of altitudes were considered with respect both the achievable performance and the feasibility aspects.

Indeed, the simplest mission scenario for NGGM consists of a single pair of satellites flying on the same orbit, with different true anomalies ("in-line" or "pearl string" formation, see Figure 2). This in-line formation samples the gravity field in the along-track direction only. On a near-polar orbit, this formation is more sensitive to gravity field variations (and mass transport) in the North-South than in the East-West direction. Therefore, a second pair of satellites must be launched in conjunction with the near-polar pair, operated in a medium inclination. This formation

composed by two pairs of satellite, one in almost polar and one in medium inclined orbit, is known as a "Bender" type formation (see Figure 2).

In the frame of the "Consolidation of the system concept for the Next Generation Gravity Mission" study, based

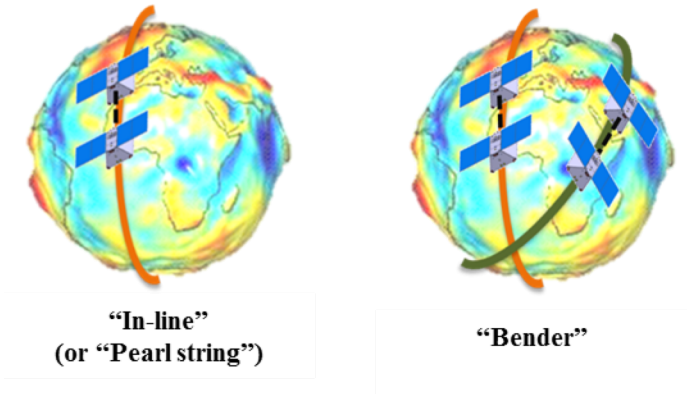

Figure 2. NGGM's satellite formations.

on the results of the scientific SC4MGV ESA's study (Ref. 4) and excluding the retrograde orbits that could not be fulfilled by the capability of the identified baseline launchers, the orbits in Table 3 have been selected for a "Bender" formation. Circular orbits, with altitudes around ~340 km, and near-polar (first pair) and medium (second pair) inclination are suitable for the NGGM Bender configuration, providing all-latitude coverage, short repeat cycles/sub-cycles and an excellent gravity signal retrieval compatible with a long lifetime.

	Near-polar	**Inclined**
β/α [rev/day]	343/22	451/29
Inclination [deg]	88	66
Altitude [km]	367.9	345.3

Table 3. NGGM's baseline orbits (2 satellite pairs).

In addition, the scientific simulation showed that the satellite formation configuration which would better perform the mission objectives consists of two satellite pairs, with an inter-satellite distance around ~100km. The near-polar orbit would be the preferred solution in case of continuity of the GRACE and GRACE-FO mission, with a single in-line orbit pair of NGGM satellites but with improved sensitivity (Ref. 4).

IV. System Concepts' Consolidation: Major Outcomes

A. NGGM System Challenges

At system level the NGGM has to face numerous challenges, summarized in Table 4. First, each satellite configuration and mass must comply with a dual-launch system. From this perspective, the baseline launcher is Vega-C. According to the ESA Science M5 information package in Ref. 6, the Vega-C maiden flight is planned in Q4 2018. Figure 3 shows the launcher performance map currently used for the preliminary studies. By interpolating this map, about 2250 kg launch performance is inferred for the most demanding orbit in Table 3, describing the Vega-C launch mass capability against the altitude and inclination of the selected orbit. Assuming a mass of about 900 kg per spacecraft, almost 450 kg are available for the dual-launch dispenser.

The second main challenge is driven by the scientific mission objectives to span a complete solar cycle that calls for at least an 11-years long mission. This long time span, together with the drag effect due to the low orbit, has a huge impact on the technology lifetime and on the propellant demand to perform the mission. As a matter of fact, the GOCE satellite flew 4 years, at an altitude lower than 260 km, with 40 kg of Xenon exploiting electric

propulsion. Therefore, an 11-year mission, even if at slightly higher mean altitude, would require more than double of the propellant mass. Moreover, the control requirements for a LL-SST mission (see Table 2) are really demanding from both the actuators/sensors and the algorithm design complexity point of view. Finally, not sun-synchronous orbits strongly affect the sensor number and accommodation, the on-board power generation and management and require a demanding thermal design.

Dual launch	→ Restricted transportable mass and satellite's envelops
11 years missions (~ 1 solar cycle)	→ Sensors/actuators/payload/structure lifetime High propellant demand to perform quasi-drag free science operations
SST Low-Low orbit	→ AOCS sensors and actuators & GNC algorithms complexity High propellant demand to perform drag free science operations
Poles coverage and high temporal resolution	→ Not sun-synchronous orbits affect sensor layout, power and thermal designs

Table 4. NGGM System Challenges.

B. Satellite Drag Coefficient Assessment and Orbits Characterization

The atmospheric drag is considered the dominant source of unpredictability for low-earth orbiting spacecraft due to uncertainty in both the knowledge of the atmosphere density and the figures of the accommodation factors of the spacecraft surfaces.

In the frame of the "Consolidation of the system concept for the Next Generation Gravity Mission" study, a dedicated analysis on the drag coefficient assessment has been carried out in order to validate the system configuration, the mission scenario, and the control algorythms. The latter rely on the TAS-I's GOCE experience in which the drag forces measured in flight were satisfactorily compared against the drag forces estimated by the NGGM end-to-end (E2E) simulator (see Figure 4), based on the heritage of the GOCE E2E Simulator. Indeed, numerical simulations (e.g. hyper-thermal and thermal models) could produce accurate estimates of the drag effect, which are computationally cumbersome for quick predictive applications, where a classical formulation accounting for constant drag coefficient is commonly used.

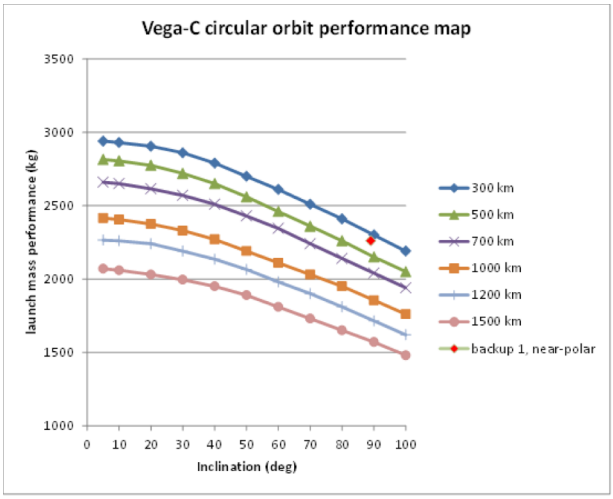

Figure 3. Preliminary Vega-C performance map.

Therefore, it has been necessary to consolidate a procedure to assess the equivalent drag coefficient (CDeq) and area (Aeq) of a flat plate perpendicular to the air stream, that best approximates the in-line perturbation force (Fx) obtainable, accounting for the GOCE/NGGM's E2E simulator thermal model.

The drag coefficient assessment follows these basic steps: (i) to derive the overall drag forces relevant to the contributes of all the spacecraft geometry's surfaces by using the free molecular flow model, (ii) to find an equivalent drag coefficient which best fits the latter model perturbations still accounting the contributes of the real satellite geometry, (iii) to find an equivalent area accounting for the overall spacecraft surfaces' contributes.

Generally speaking, it is reasonable to expect the equivalent drag coefficient to be larger than the best fit single-surface and the physical frontal area, because the flat plate model incorporates the force contributions produced by the lateral surfaces of the satellite (for instance, in GOCE, ESOC – the ESA satellite control center - found that the orbit data were best fit by $CDeq \cdot Aeq = 3.5\ m^2$).

Interestingly, for the NGGM satellite a higher value of the equivalent drag coefficient with respect to the GOCE one has been found, this is due mainly to the different spacecraft geometry. Indeed, it has been evaluated that, for

the NGGM satellite configuration shown in Figure 5, the contribution of all the wing planes accounts for about half of the total drag force.

Consequently, given the set of orbits described in Table 3, and applying the obtained equivalent area and drag coefficient, the drag analysis has been performed for different starting epochs. This aspect was defined to encompass different levels of solar activity, in order to analyse all the possible conditions at which each satellite would be exposed during its operational lifetime. As expected, a condition of maximum solar and geomagnetic activity leads to higher drag force values that can differ up to 3÷4 mN from the drag force experienced during minimum activity conditions. Finally, the wide range of simulations highlighted that both altitude and inclination play a role in defining the atmospheric density levels, being altitude the major driver.

C. Required Thrust and Layout/Dispatching Optimization

One of the main drivers of the NGGM mission is the required thrust authority to perform a mission of 11 years. In turn, the thrust authority has impacts on both technological and control sides. Therefore, a methodology aimed at finding a thruster layout able to cope with the low/medium/high atmosphere conditions, and that minimizes the mission fuel consumption, has been studied and designed in the on-going "Consolidation of the system concept for

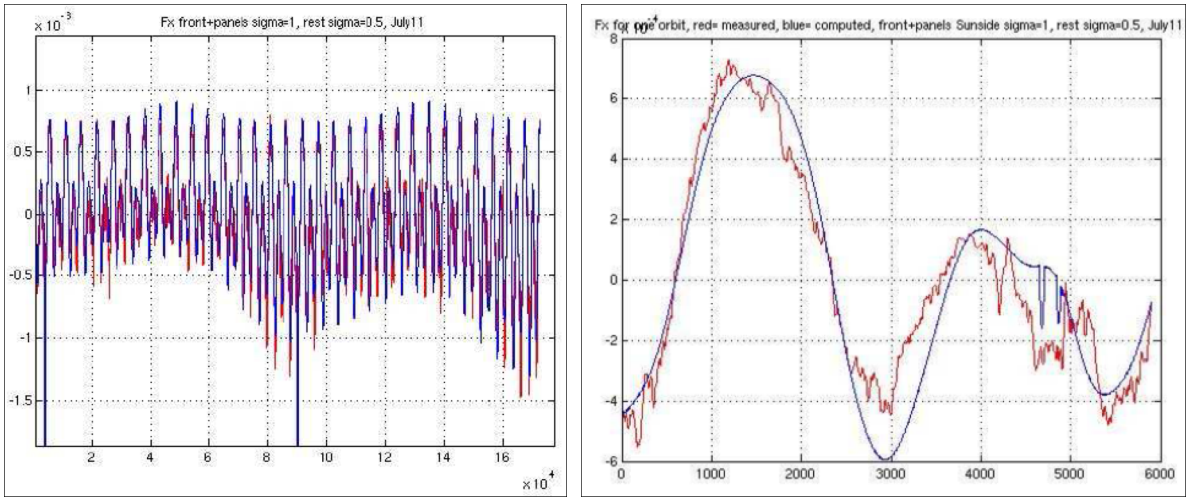

Figure 4. GOCE drag force along the in-line Force: calculated by the E2E simulator (blue line), measured in flight (red line), July 2011

the Next Generation Gravity Mission".

Three operational scenarios of the aforementioned atmospheric conditions define the analysis framework. For each scenario, a statistical representative sample has been considered and the required control force/torque has been evaluated, during the scientific mission. This force/torque demand led to the optimal thruster layout assessment.

As stated previously, the major contributor to the overall requested thrust, in the mission Scientific Mode, is due to the along-track drag compensation. In the previous NGGM AOCS study of Ref. 3, the control force/torque dispatching relied on the classical Moore-Penrose inverse matrix which calls for a symmetric "not-optimal" thruster layout. In the frame of the on-going system study, a more general optimization problem has been defined by considering the thrusters mounting positions and orientations aimed at minimising the fuel consumption. The potential of this new optimal thruster layout and dispatch optimization method are illustrated in comparison with the previous symmetric layout in Figure 6. As highlighted in Figure 6, the optimized layout and dispatching reduce the propellant needed from 15% to 27% depending on the solar activity, while equalizing the thrust distribution among the 8 thrusters. The estimated reduction of the total impulse required to the micro-thrusters (i.e. mini-GIE) varies from 26% up to 73%.

D. Technological Innovations

As far as a scientific mission as the one presented (see Paragraph II.B) is concerned, on top of an innovative system design, some not trivial technological innovations are needed.

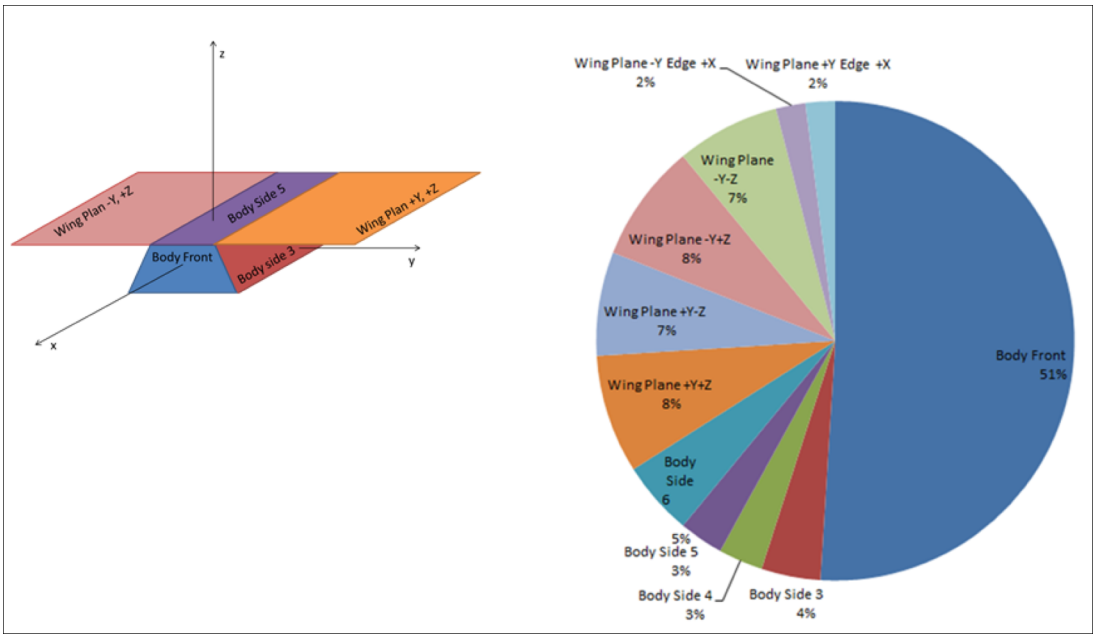

Figure 5. NGGM surfaces' contributions to the overall drag force.

Specifically, the spacecraft propulsion is the major open issue of the NGGM design. An interesting outcome of the several system studies is that the thrust range and modulation capability imposed by the mission requirements and objectives, coupled with the lifetime requirement, imply the use of electric propulsion (EP). In turn, the EP

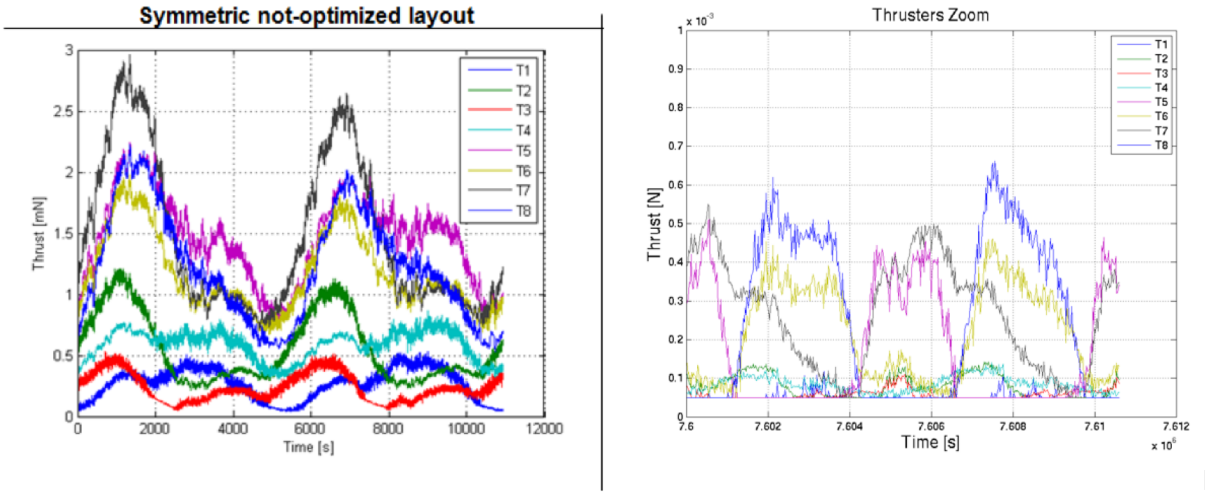

Figure 6. Symmetric layout and Moore-Penrose dispatch (left) vs. optimed layout and dispatching (right). Comparison in case of 8 thrusters, with the same thrust range and ISP, over two orbits in science mode (zoom on the right figure), near-polar inclination, min solar activity.

makes the mission feasible because of an optimized high specific impulse, reducing the propellant mass requirements. However, in this configuration, the s/c mass is traded for electric power, and kW-level power generation is itself not a trivial task in a mission that needs to keep the drag cross section small with a highly variable solar aspect angle. In addition, high specific impulse is normally only available over a limited thrust range. This could imply the use of different thruster types for different tasks (e.g. along-track drag control, 3-axis attitude and drag free angular control, orbit maintenance, formation acquisition, and orbit manoeuvres). All this, in turn, must be achieved while respecting the stringent system limitations in terms of mass, volume, and power.

Thus, the optimal implementation of the NGGM propulsion turns out to be a complex system trade-off involving:

1. optimal balancing of dynamic and control needs vs. orbit altitude (possibly considering a variable-altitude mission);
2. system mass and power limits;
3. propulsion reliability vs. lifetime vs. number of units.

From the payload point of view (not treated in this paper), the laser metrology is the major driver of the system design due to the accommodation requirements, the positioning of the laser duct, the pointing and pointing-stability requirements and the environment thermal control requirements. In fact, the distance variation between the centres of mass of the satellites (see Δd in Figure 1) produced by all the forces (gravitational and not) acting on each spacecraft is the first fundamental observable of the SST technique. The NGGM scientific objectives can be achieved if Δd is measured with an error spectral density (SD) below the limit shown in Figure 7. For an inter-satellite distance of 100 km, this implies a relative measurement error $<2\cdot10^{-13}$ $1/\sqrt{Hz}$ down to a frequency of 10 mHz. This outstanding performance can be achieved only using a laser interferometer fed by a source stabilized in frequency to better than the specified relative measurement error. In particular the laser metrology concept has to minimize:

1. the laser frequency noise;
2. the phase noise from any signal path outside to the actual satellite-to-satellite measurement track (SST, see Figure 1);
3. the phase noise in SST path;
4. the satellite pointing noise.

The extent to which the design considerations stated above drive the system depends on the interferometer sensitivity to each error term: proper error budgets are in preparation and account for all the noise sources at instrument and platform level. In addition the whole system needs to fulfil, as for the thruster subsystem, the mass, power and the reliability requirements.

V. AOCS Architecture for Two Satellite Pairs in "Loose" Formation

The AOCS architecture is based on the so called Embedded Model Control methodology (EMC), which implies the design of an internal model (i.e. the Embedded Model) coded into the control unit and running in parallel to the real plant. The Embedded Model is made up by two main building blocks: the controllable dynamics of the plant to be controlled (i.e the spacecraft), completed by a disturbance dynamics model. EMC allows to treat all the wide range of unmodelled dynamics, non-linear effects and parameter uncertainties as disturbances, collocated at the command level, which can be estimated and rejected. We leave to the reader the insights on the EMC methodology, given in Ref. 8-10, and we recall the main driving principles injected into the AOCS design:

Integrated *orbit* and *formation* control. The control design is driven by an innovative approach to multi-satellite formation control based on the integration of the orbit and formation dynamics and control through the formation triangle concept (described in the subsection V.B). As a matter of fact, such modelling idea leads to new Clohessy-Wiltshire (CW)-type equations (see Ref. 9).

Frequency coordination. The drag compensation system (commonly and ideally called "Drag-Free control") and the formation control are actuated at different frequency bands. This is deemed necessary in order to prevent any possible interference among inner/outer loops control functions and to coordinate properly the several tasks of the control design.

Multi-hierarchical control. The control tasks are carried out via a multi-hierarchical control design (see Figure 8). Indeed, the integrated orbit and formation control is an outer loop which provides the long-term reference accelerations to be tracked by the drag-free control.

Attitude and formation decoupling. At a first approssimation, the control frame and formation local orbital frame (the so-called FLOF frame) can be considered as matching, since the early mission phases. Nevertheless, some coupling still persists for the (single) satellite attitude control with respect to the FLOF, at certain extent due to the thruster dispatching algorithm and to a very limited thrust authority.

Coordinate decomposition applies to all the control blocks of Figure 8. For instance, the drag-free control is

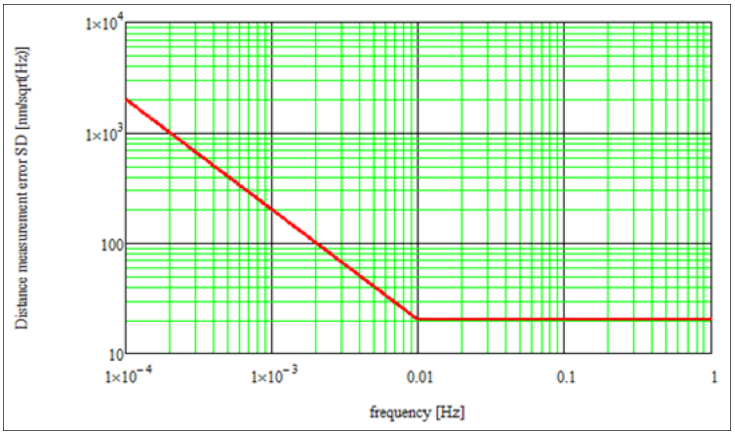

Figure 7. Specified inter-satellite distance variation measurement error.

decomposed into six independent SISO (single-input-single-output) loops, 3 for the linear and 3 for the angular drag-free, taking advantage of the stochastic disturbance dynamics. Specifically, concerning the attitude and pointing, the coordinate decomposition (roll, pitch, and yaw) relies on the assumption of small (order of mrad) estimation and tracking errors, since the early mission phases. Nevertheless, the formation embedded model is not completely decoupled, because of the interactions between the altitude and the distance, coherently with the longitudinal and the radial coupling described by the CW's equations.

A description of the linear and angular drag compensation control, together with the orbit and formation control is provided in V.A and V.B, whereas the attitude control is treated here in V.C, considering that the basic principles of the design of the attitude control are extensively covered in Ref. 3.

A. Linear and Angular Drag-Free Control

The Drag-Free linear control aims at making the satellites orbit only affected by the local gravity. Therefore, the satellite formation is ideally only subjected to differential accelerations due to gravitation, which are revealed by the inter-satellite distance fluctuations. Notwithstanding some secular (low frequency) residual accelerations will affect the satellites orbit, due to the accelerometer intrinsic errors (bias, drift, etc.). On the other side, the angular drag-free control aims at zeroing all the disturbance torques, including gyroscopic, gravity gradient, magnetic, and aerodynamic torques. In the conceived all-electric platform design, both the commanded force and torques are actuated by a thruster assembly. Given the impossibility of an ideally perfect drag-free condition, due to the accelerometer errors above mentioned, formation and attitude controls are needed.

From the system perspective, each drag-free satellite, according to the accelerometer concept illustrated in Ref. 7, embarks a proper cage with proof masses. In addition, an active suspension system, after performing initial centering after launch, keeps the masses centered in the cage. As a consequence, by measuring the suspension force, it is possible to retrieve a measurement of the non-gravitational forces acting on the satellite, which can be directly cancelled – to a certain extent - by the thrusters commanded by the drag-free control.

The ideal drag-free requirement, both concerning the linear and the angular case, is to zero the residual accelerations in the selected MBW. Outside this frequency interval, the requirement may be relaxed in order to accommodate the formation and attitude control authorities. The Drag-Free control is actuated separately on each satellite of the NGGM formation. Considering a single satellite, the EMC allows each component to be controlled separately, leading to six decoupled scalar drag-free controls for each spacecraft (three for the linear and three for the angular cases).

The Embedded Model includes a disturbance dynamics model of the disturbance class affecting the dynamics, driven by arbitrary unknown signals. Such a disturbance estimation model is designed based on experimental data and literature about thermosphere density and experimental thruster noise. The studies made during the ESA GOCE mission (Ref. 7) suggested how a combination of white noise (accounting for the thruster noise), and a first and second-order random drift (modelling the thruster noise and the aerodynamic forces) is a reliable stochastic model for the class of the expected time realizations. As a consequence, according to the Embedded Model Control methodology, a ninth-order stochastic disturbance dynamics (third order for each axis) driven by a 12th-dimensional bounded noise vector $\mathbf{w}_d$, allows to reliably account for the high frequency spectral density of drag, thruster noise, and accelerometer bias/drift (Ref. 9). The final DT model of the sensor-to-actuator dynamics, which is embedded in the control unit, is

$$\begin{aligned}\mathbf{x}_a(\mathrm{i}+1) &= \begin{bmatrix} 0 & I & 0 & 0 \\ 0 & I & I & 0 \\ 0 & 0 & I & I \\ 0 & 0 & 0 & I \end{bmatrix}\mathbf{x}_a(\mathrm{i}) + \begin{bmatrix} I \\ 0 \\ 0 \\ 0 \end{bmatrix}\mathbf{u}_a(\mathrm{i}) + I_4\mathbf{w}_d(\mathrm{i}), \\ \mathbf{y}_a(\mathrm{i}) &= \begin{bmatrix} I & 0 & 0 & 0 \end{bmatrix}\mathbf{x}_a(\mathrm{i}) + \mathbf{e}_a(\mathrm{i})\end{aligned} \tag{3}$$

where the state vector is $\mathbf{x}_a = \begin{bmatrix} z_a & x_d & s_d & z_d \end{bmatrix}^T$, $\mathbf{u}_a$ is the command, $\mathbf{e}_a$ is the model error (plant minus model output), $\mathbf{w}_d$ is the noise signal driving the disturbance dynamics. The first state of the state vector $\mathbf{x}_a$ accounts for the delay, i.e. the simplified thruster-to-accelerometer dynamics. Then the second state $\mathbf{x}_d$ is the output of the disturbance estimation dynamics, intended to provide, inter alia, a reliable estimate of the total gravitational effects. As a consequence, if the total acceleration reads

$$\mathbf{a}(\mathrm{i}) = \mathbf{d}_a(\mathrm{i}) + \mathbf{b}_a(\mathrm{i}) + \mathbf{u}_a(\mathrm{i}), \tag{4}$$

where $\mathbf{d}_a(\mathrm{i}) + \mathbf{b}_a(\mathrm{i})$ is the sum of the total estimated disturbances and the accelerometer secular error (bias/drift), it can be written

$$\mathbf{d}_a(\mathrm{i}) + \mathbf{b}_a(\mathrm{i}) = \mathbf{x}_d(\mathrm{i}) + \mathbf{w}_d(\mathrm{i}), \tag{5}$$

The loop is closed by adding to Eq. 3 a static noise estimator, as in standard observers

$$\mathbf{w}_d(\mathrm{i}) = \mathbf{L}\mathbf{e}_a(\mathrm{i}) \tag{6}$$

where a $\mathbf{L}$ is a 12×3 constant matrix, making the closed-loop dynamics asymptotically stable. The non-zero entries (on the diagonal) of $\mathbf{L}$ are computed by assigning the eigenvalues of the closed-loop matrix trading-off stability property vs. the desired performance level.

It is worth to notice how in Eq. 3 the sensor-to-actuator dynamics is simplified to a first-order dynamics (first row in Eq. 3): such a design simplification in the Embedded Model is in line with the GOCE drag-free control of preparatory phases in Ref. 7.

From the control perspective, being the thruster-to-accelerometer dynamics in Eq. 3 asymptotically stable, the reference tracking is ensured by only cancelling at the better extent the sum of the estimated disturbance $\mathbf{d}_a(\mathrm{i}) + \mathbf{b}_a(\mathrm{i})$. Therefore, the control law is

$$\mathbf{u}_a(\mathrm{i}) = -\mathbf{x}_d(\mathrm{i}) + \mathbf{u}_{ref}(\mathrm{i}). \tag{7}$$

According to the drag-free control concept, the former term in Eq. 7 tends to ideally zero the non-gravitational accelerations, within the selected bandwidth. The second term generically denotes either formation or attitude commands, counteracting the drag-free residuals.

B. Integrated Orbit and Formation Dynamics and Control (IFC)

The designed orbit and formation embedded model assumes that the high-frequency forcing accelerations are only due to the gravity secular components. As a matter of fact, this assumption is due to the high-frequency drag-free control action, able to cancel the short-term non-gravitational accelerations. In the present design, as soon as the formation distance can be on-board controlled, formation and orbit control are combined into a unique strategy, through the definition of the formation triangle virtual structure (Figure 9 and Ref. 9) and of the frame perturbations. By design, the formation triangle vertices join the satellites CoM and the Earth CoM. The model has been built with respect to the common main frame of reference, namely the Formation Local Orbital Frame (FLOF). The three FLOF axes are defined as follows

$$\mathbf{o}_1 = \frac{\Delta\mathbf{r}}{d}, \qquad \mathbf{o}_2 = \frac{\dfrac{\mathbf{r}}{r}\times\mathbf{o}_1}{\left|\dfrac{\mathbf{r}}{r}\times\mathbf{o}_1\right|}, \qquad \mathbf{o}_3 = \mathbf{o}_1\times\mathbf{o}_2, \tag{8}$$

where $\mathbf{o}_1$ is the satellite-to-satellite (SSL) direction, $\mathbf{r}$ is the mean formation radius, $\Delta\mathbf{r}$ is the satellites relative position, and d is the inter-satellite distance.

As a consequence, the orbit/formation dynamics is expressed through a combination of Cartesian and angular perturbations (triangle angular rotations), defined through the FLOF frame. Specifically, the three controllable Cartesian perturbations (see Figure 9) are: (i) the distance variation δd, (ii) the formation mean radius deviation (along the SSL) δr_x, (iii) the mean altitude variation δr_z, defined according to

$$\Delta\mathbf{r} = (\mathrm{d}_{nom} + \delta d), \qquad \mathbf{r} = (r_{nom} + \delta r_z)\mathbf{o}_3 + \delta r_x \mathbf{o}_1, \tag{9}$$

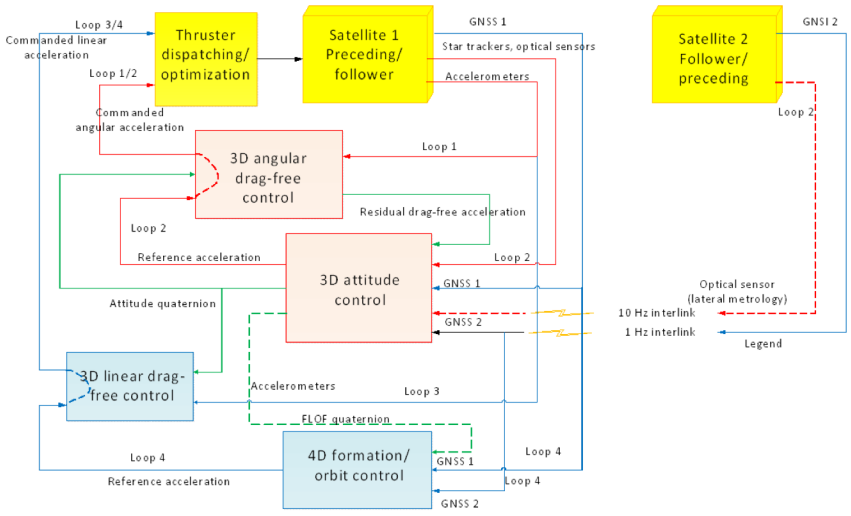

Figure 8. Higher-level block diagram of the AOCS architecture for the NGGM science mode.

given the nominal radius r_{nom}, and the nominal inter-satellite distance d_{nom}.

The resulting integrated orbit and formation dynamics is expressed through a new set of CW-type equations, based on the differential equations of the formation triangle perturbations (as in Ref. 9). In order to derive these equations of motion, starting from the relative satellites position vector, we have derived the differential equations of the inter-satellite distance and their derivatives. After that, the formation triangle kinematic equations in terms of the FLOF angular rate and of the angular acceleration have been obtained, as per Ref. 9.

It is worth to notice how the gravity gradient has been kept into account, in first approximation for a spherical gravity potential field. Indeed, the higher order terms, referring to non-uniform gravity forces acting on extended bodies, have been considered as external disturbance accelerations. Such a model linearization leverages the Embedded Model Control capability to estimate and reject in the control law all the non-explicitly modelled effects, through the disturbance dynamics. The set of differential equations is completed by the six formation degrees of freedom concerning the mean and differential altitude.

As already mentioned, the rationale behind the orbit and formation control is to counteract the drag-free residuals. Indeed, given a formation variable, the distance d, can be decomposed as the sum of three terms: (i) a nominal value d_{nom}, (ii) a secular component d_0, and (iii) a periodic component d_g, due to the real gravity field. The third component d_g is linked to the scientific product of the mission whereas the second one d_0 is due to the accelerometer errors (i.e. bias/drift), preventing a perfect drag-free control action. Hence, the orbit and formation control has been conceived as an outer loop aiming at regulating the formation variables to their nominal value, and neglecting the periodic component while trying to zero the secular one. As a consequence, starting from the above mentioned set of differential equations, the perturbation equations - linearized around the equilibrium point - can be adopted for the control design purpose.

The next modelling step leads to the discretization of the equations to be implemented within a digital control unit. The discretization step must take into account that the formation control authority should not degrade the Drag-Free requirements taking in account the very limited thrust authority. For this purpose, a continuous control strategy appears to be useful (Ref. 9): as a matter of fact, the orbital rate has been valued as a viable discretisation time step. Hence the IFC command changes at each orbit period.

The embedded model encompasses the controllable model (i.e. the ZOH DT formation equations) completed by a purely stochastic and parameter-free disturbance dynamics, describing the secular components (bias and drift) of the unknown disturbances. To build the controllable dynamics part, all the uncontrollable variables as the longitudinal perturbation and the formation rates have been dropped, since we are only interested in the control of the formation triangle position variables (radial and altitude control). In the following, for the brevity sake, only the discrete-time final equations of the formation internal model are provided.

Let us define the state vector of the orbit and formation integrated model (IFC) as

$$\mathbf{x} = \begin{bmatrix} \mathbf{r}_w & \mathbf{w} \end{bmatrix}^T = \begin{bmatrix} \rho_{xw} & \rho_{zw} & d_w & \theta_w & w_x & w_z & w_d & w_y \end{bmatrix}^T \tag{10}$$

where the terms w_k are the four normalized formation rate perturbations, while $\rho_{xw} = \rho_x + (w_d - w_z)/2$, $\rho_{zw} = \rho_z + (w_y + w_x)/2$, $d_w = \delta d + \rho_z + 2w_y$, $\theta_w = d_{nom}\delta\theta - 3\rho_x - 2w_d$ are linear combinations of formation position perturbation variables ($\rho_x = \alpha\delta r_x$, $\rho_z = \alpha\delta r_z$), where $\alpha = d_{nom}/r_{nom}$ is an adimensional scale factor. Hence, the linearized secular formation dynamics DT Embedded Model (controllable plus first-order disturbance dynamics) reads

$$\begin{bmatrix} \mathbf{r}_w \\ \mathbf{x}_d \end{bmatrix}(\mathrm{i}+1) = \begin{bmatrix} A_w & I \\ 0 & I \end{bmatrix}\begin{bmatrix} \mathbf{r}_w \\ \mathbf{x}_d \end{bmatrix}(\mathrm{i}) + \begin{bmatrix} B_w \\ 0 \end{bmatrix}\mathbf{u}(\mathrm{i}) + \begin{bmatrix} \mathbf{w}_r \\ \mathbf{w}_d \end{bmatrix}(\mathrm{i}),$$

$$\begin{bmatrix} \mathbf{r}_w \\ \mathbf{x}_d \end{bmatrix}(0) = \begin{bmatrix} \mathbf{r}_{w0} \\ \mathbf{x}_{d0} \end{bmatrix} \quad \mathbf{y}(\mathrm{i}) = \begin{bmatrix} I & 0 \end{bmatrix}\begin{bmatrix} \mathbf{r}_w \\ \mathbf{x}_d \end{bmatrix}(\mathrm{i}) + \mathbf{e}_m(\mathrm{i}),$$

$$A_w = \begin{bmatrix} 1 & 0 & 0 \\ 0 & 1 & 0 \\ -12\pi & 0 & 1 \end{bmatrix}, \quad B_w = \begin{bmatrix} 0 & -\alpha/2 & 1/2 & 0 \\ \alpha/2 & 0 & 0 & 0 \\ 0 & 3\pi\alpha & -3\pi & -2 \end{bmatrix}\frac{T_0}{\omega_{nom}} \tag{11}$$

In Eq. 11, $\mathbf{r}_w$ is the controllable part of the state vector (comprising the three states relatively to the distance variations, the mean altitude and formation mean radius deviation). The input variable $\mathbf{u}$ is given in acceleration units. In Eq. 11 all the state variables are decoupled except the lateral perturbation pair d_w, and ρ_{xw}. $\mathbf{x}_d$ is the disturbance state sub-vector expressing the unknown disturbance dynamics states: in order to describe the secular components (bias and drift), three first-order stochastic dynamics were added. In addition, $\mathbf{w}_r$ and $\mathbf{w}_d$ components play the role of arbitrary but bounded signals driven by the model error (plant minus model output) $\mathbf{e}_m$. Thus, the loop is closed completing the state predictor by adding a static noise estimator to the embedded model, as per Eq.12.

$$\mathbf{w} = L\mathbf{e}_m, \quad \mathrm{L}=\begin{bmatrix} L_x & 0 \\ 0 & L_z \end{bmatrix}. \tag{12}$$

The elements of the diagonal matrix $L \in \Re^{6\times 3}$ are scalar gains that can be tuned via pole placement, by fixing the closed-loop eigenvalues. This allows a trade-off between a fast disturbance prediction and the closed-loop predictor stability.

Extensive simulations, in Ref. 3 and 9, have shown the IFC model to be satisfyingly robust to the initial orbit perturbations envelope, along the science phase of the NGGM mission. Indeed, given the very low thrust level constraining the NGGM control design (few milli-Newtons), stability and drift issues may affect some formation variables in case of a set of non optimal initial conditions after the transition from the coarse to the science mode. Specifically, issues of this kind can arise after: (i) poor/missing formation and orbit acquisition, (ii) large errors due to the transition from pre-science control modes.

At the time of writing, a possible improvement of the formation control is under consideration, where the GNSS paramenters are not transmitted via an inter-satellink link, imposing constraints in the design and in the satellite testing, but propagated along the orbit after having been uploaded via TM/TC.

1. IFC Control Synthesis

In this section, the synthesis of the IFC control law will be addressed. We recall that the total linear control action is organized in a hierarchical way: the inner loop is the drag-free control (see Section V.A), while the outer loop is the orbit/formation control. The actuation time is sampled at the shortest time unit $T = 0.1s$ which is imposed by the drag-free control. Therefore, at each control step, the drag-free command is dispatched to the plant, while, at each navigation or orbital step, the IFC part of the command adds up to the drag-free one.

Concerning the IFC, the control algorithms are organized around the above described embedded model of Section V.B. The IFC control law is the combination of a feedback term and of a disturbance rejection term. First of all, the disturbance rejection term is responsible for the embedded model stabilization: given the unitary eigenvalues

of the disturbance dynamics in Eqs. 11, the rejection of the estimated disturbances is needed to make the closed-loop system BIBO stable. Secondly, the IFC feedback command portion is the result of two combined control strategies: the proposed solution is a multi-hierarchical structure of the feedback control law able to prevent that the formation rate variables, uncontrollable by the low-frequency control of the DT IFC in Eqs. 11, could affect the controllable

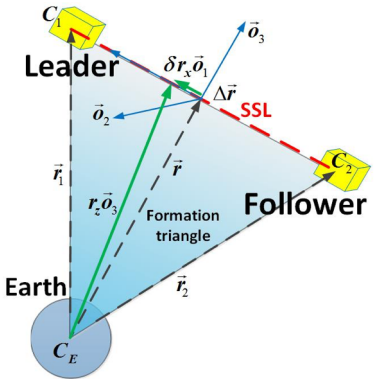

Figure 9. The formation triangle and the Formation Local Orbital Frame (FLOF).

variables stability, when closing the loops in some orbital conditions. Therefore, the feedback encompasses:

(i) an orbit and formation stabilization, through the designed low-frequency (orbital) formation position feedback, plus

(ii) a further stabilizing feedback loop to ensure a proper damping of the formation variables eventually drifting.

As a result, on the one hand, the position feedback operates at the orbital frequency and stabilizes the long-term perturbed dynamics of the formation triangle. Such feedback component leverages the state variables recovered by the state predictor (see Eqs. 11 and 12), starting from the available measurements. On the other hand, a formation rate damping control, operating at the time unit of the navigation data, damps suitably the formation rates components which have been found to affect the formation stability. As a further notice, the rate damping control loop is directly fed by formation rates measurements, obtained from the navigation data, without any state predictor.

The IFC control law synthesis results in

$$
\begin{aligned}
&\mathbf{u}_{IFC}(\mathrm{i}) = -B_w^{-1}\left[K_w \mathbf{y}_w(\mathrm{i}) + \left(K_r \mathbf{r}_w(\mathrm{i}) + \mathbf{x}_d(\mathrm{i})\right)\right],\\
&K_w = \omega_{nom}\,\mathrm{diag}\left\{\zeta_x, \zeta_z, \zeta_d, \zeta_w\right\},\\
&\zeta_d = 2.8e-7, \quad \zeta_x = \zeta_z = \zeta_w = 0,\\
&K_r = \begin{bmatrix} \gamma_x & 0 & 0 \\ 0 & \gamma_z & 0 \\ -12\pi & 0 & \gamma_d \end{bmatrix}
\end{aligned}
\tag{13}
$$

where $\mathbf{y}_w$ are the formation rate variable measurements, $\mathbf{x}_d$ and $\mathbf{r}_w$ are respectively the disturbances to be rejected and the controllable states prediction, both coming from Eqs. 11. Further, the tuning of the control action is pursued via the rate K_w and position K_r feedback gains matrices. Finally, the command is dispatched to the plant through the pseudo-inverse $B_w^{-1} \in \Re^{6\times 3}$ of the command matrix ($B_w \in \Re^{3\times 6}$ in Eqs. 11).

It is worth to notice that the reference part of the command is missing in Eqs. 13 because the state variables have been defined as perturbations with respect to the reference value.

The choice of the preliminary control gains in Eqs. 13 was carried out via a pole-placement procedure and then refined in simulation. Specifically, the gain matrix K_r is fixed by assigning the eigenvalues of the closed-loop matrix $A_w - B_w K_r$, being the tracking error in Eqs. 13 bounded and zero-mean if and only if $A_w - K_r$ is asymptotically stable. Furthermore, the rate feedback portion (through K_w) must be optimised, given the very limited thrust authority constraining the control design. As a result, in a preliminary configuration, only the formation distance rate is proposed to be fed back (gain $\zeta_d \neq 0$). Such preliminary choice, also coming from the most representative and typical in-ine long-run scenarios, was proven to ensure long-term stability as well as minimum acceptable values within the required thrust authority.

Figure 10 provides a sketched representation of the IFC control unit block diagram. The embedded model structure is clarified (controllable plus disturbance dynamics) while the noise estimator feedback closes the loop of the formation state predictor. The control law block receives its inputs both from the embedded model and the navigation sensor. The measurements received by the state predictor are pre-processed in order to filter out the periodic components due to the Earth gravity field.

C. Attitude and Pointing Control (APC)

The design of the attitude and pointing control (APC) is still based on a proper embedded model, assuming that the angular accelerations are counteracted (ideally cancelled) by the angular drag-free control. As a matter of fact, this assumption is due to the high-frequency drag-free control action, able to cancel the short-term angular accelerations. Therefore, similarly to the integrated orbit and formation control case (in V.B), an effective attitude and pointing control is needed in order to counteract the effects of the accelerometer errros (mainly bias and drift). From the sensor perspective, the APC control unit receieves its inputs from the several attitude sensors made available by the NGGM P/F sensort suite. From this perspective, star trackers provide the S/C absolute attitude, mainly adopted in the early mission phases (with less stringent attitude and pointing requirements). On the other side, on-purpose designed optical metrology sensors - providing the S/C optical axis misalignment with respect to the satellite-to-satellite line - are employed for the mission Science model control algorithms. Indeed, in Science mode, the APC has to ensure the alignment of the satellites optical axis (SSL), to enable the measurement - via laser interferometry - of the inter-satellite distance variations, i.e. the scientific observables of such future gravity mission.

The adopted design still requires a radio interlink (ISL) to exchange GNSS and attitude data, leveraged to build the NGGM formation attitude reference generator and predictor. Figure 8 provides also an overbiew of the APC controller rationale and interfaces with the rest of the control unit: specifically, we notice the input/output signals, the interlink, and the APC control being an outer loop which provides the long-term reference accelerations to be

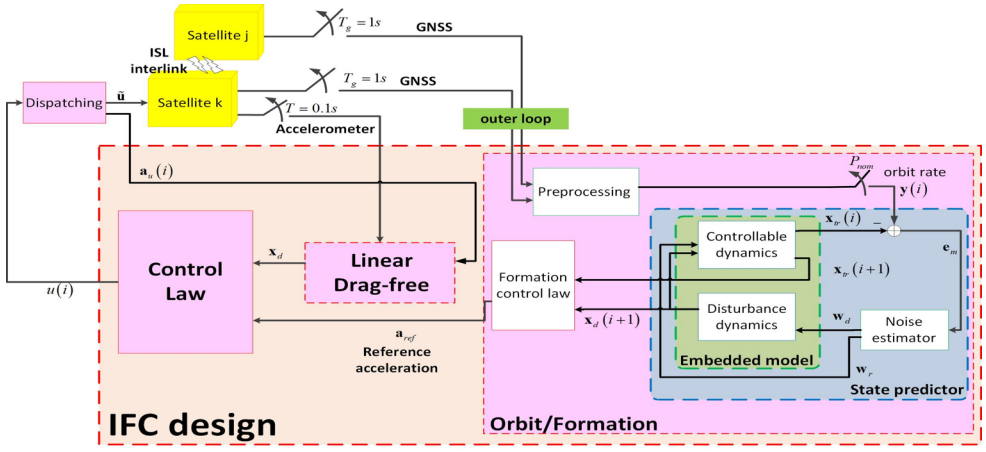

Figure 10. Overall scheme of the Integrated Formation Control.

tracked by the angular drag-free control. Furthermore, the attitude control is actuated by the same propulsion assembly responsible for the IFC control action, hence no pointing mechanism to steer the laser beam is foreseen, coherently with the most updated platform system architecture.

Generally speaking, the formation attitude rationale pursues an independent pointing control for each satellite, where the control design is based on the attitude kinematics and dynamics equations detailed with respect to: (i) a suitable control reference frame, whose origin is in the S/C CoM, and (ii) the common FLOF frame. For the sake of completeness, the control frame, which can be assumed as almost coincident with the S/C body frame, has one axis defined via the optical metrology assembly, in the along-track direction, plus another axis close to the cross-track accelerometer pair direction. As a result, we can define two reference quaternions, namely a control quaternion q_{ck} (defining the absolute attitude of the satellite), and the FLOF one q_o (defining the FLOF absolute attitude). Hence, being the control objective the alignment of the S/C to the SSL, the control quaternion should be aligned to the FLOF one, thus allowing the error quaternion definition q_k, as:

$$q_k = q_o^{-1} \otimes q_{ck}, \tag{14}$$

defining the relative orientation of the S/C with respect to the FLOF orbital frame. In turn, the attitude quaternion kinematics and the satellite dynamics driving the model-based APC controller are based on the relative quaternion in Eq. 14. Specifically, the attitude control unit is based on a discrete-time version of the relative quaternion kinematics and S/C dynamics; to this aim, the APC controller is based on two embedded models as described in Ref. 13-14: (i) th FLOF embedded model, and (ii) the relative attitude embedded model. The FLOF embedded model consists of the q_o kinematics, plus a third order stochastic angular rate model, where the state variables are the angular rate, the angular acceleration and the jerk, providing the reference attitude, angular rate and accelerations to the S/C (for guidance purposes). Conversely, the relative attitude Embedded Model relies on the q_k kinematics, also augmented with third order disturbance equations (as the FLOF one), but also with the attitude command and the explicit FLOF acceleration: it predicts the S/C attitude and angular rate. Finally, as above described, the two embedded models are made closed loop via a noise estimator, providing the output-to-state feedback, so to have a closed-loop state predictor of the embedded model states (controllable plus disturbance). However, differently from Eqs. (3) and (11), the attitude predictor cannot be designed and stabilized via a static noise estimator, as in Eq. (12), due to the state vector dimension being higher than the input noise signals. Therefore, in both cases, the formulation in Eq. (12) is augmented with a first order dynamics (adding an extra state variable $\mathbf{p}_q$), i.e.:

$$\begin{aligned} \mathbf{p}_q(\mathrm{i}+1) &= (1-\beta_q)\mathbf{p}_q(\mathrm{i}) + \mathbf{e}_q(\mathrm{i}), \\ \mathbf{w}_q(\mathrm{i}) &= L_q\mathbf{e}_q(\mathrm{i}) + M_q\mathbf{p}_q(\mathrm{i}), \end{aligned} \tag{15}$$

where the the gain matrices L_q and M_q, being multidimensional to account for the three control axes, are the equivalent of L in the static noise estimator in Eq. (12), and together with β_q broaden the number of the closed-loop tunable parameters, for each axis. Thus $\mathbf{w}_q$ components play the role of arbitrary but bounded signals driven by the relative attitude model error $\mathbf{e}_q$ and closing the state predictor loop.

Finally, the total angular control law $\mathbf{u}_{APC}$ is the sum of the drag-free control action $\mathbf{u}_{df}$, and the attitude and pointing one $\mathbf{u}_{ref}$, coherently with the total linear command in Eq. (7). Hence, it holds:

$$\mathbf{u}_{APC}(\mathrm{i}) = \mathbf{u}_{df}(\mathrm{i}) + \mathbf{u}_{ref}(\mathrm{i}),$$

$$\mathbf{u}_{df}(\mathrm{i}) = -\mathbf{x}_{d}(\mathrm{i}), \qquad \mathbf{u}_{ref}(\mathrm{i}) = -\left(\mathrm{K}_{q}\,\mathbf{e}_{q}(\mathrm{i}) + \mathrm{K}_{v}\,\mathbf{e}_{v}(\mathrm{i})\right) - \mathbf{x}_{qd}(\mathrm{i}) + \mathbf{a}_{o}(\mathrm{i}), \tag{16}$$

where the APC control law $\mathbf{u}_{ref}$, sampled at the time unit of the drag-free, is made up by: (i) the attitude predicted disturbance rejection (estimated accelerometer bias/drift) $\mathbf{x}_{qd}$, (ii) the orbital FLOF acceleration reference command $\mathbf{a}_{o}$ (predicted by the FLOF embedded model), and (iii) the state feedback, based on the quaternion and rate model errors, respectively $\mathbf{e}_{q}$ and $\mathbf{e}_{v}$, with the control gains (K_{q}, K_{q}) to be propely tuned to reach the final tracking performance.

VI. Simulated Results

This section will present some relevant simulated results for the inline orbit loose formation, obtained through an E2E high-fidelity mission simulator including the complete control unit. The first 32 harmonics of the Earth gravity field spherical harmonics expansion have been simulated together with an Oersted geomagnetic field model (order 18) and mean solar activity conditions, if not differently specified. At system level, all the sensor and actuator dynamics are active and their noises are modeled. Parametric uncertainty affect the several sensor parameters as well as the thruster assembly parameters.

Figure 11 shows the unilateral spectral density of the linear acceleration residuals versus the performance requirement. The PSD profile is such to respect the requirements. The low-frequency overshoot appears to be linked to the formation transient. Similarly, simulated results showed how the cross-track PSD component (in green in Figure 11) is heavily affected by the differential GNSS model noise, thus approaching the requirement bound. As anticipated, there could be room for improvements both at the system and control level removing the ISL, relaxing the differential GNSS requirements in favour of a different acquisition and pointing metrology system (APMS): investigations on these aspects are on-going.

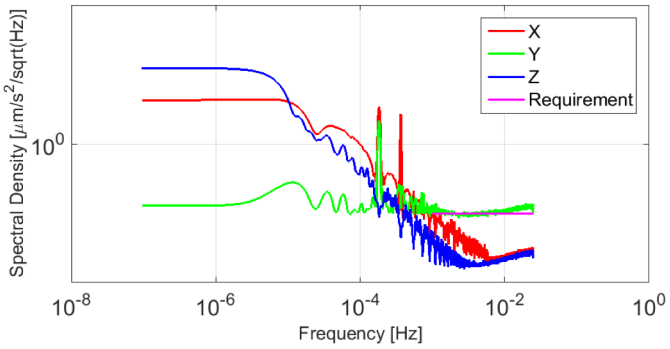

Figure 11. Simulated PSD of the linear non-gravitational residuals

Figure 12 shows the unilateral spectral density of the angular acceleration residuals versus the performance requirement. The requirement bound is met with some margin. Figure 13 depicts the formation triangle position variables time history (distance variation δ_{d}, mean altitude r_{z} and formation mean radius deviation along the SSL r_{x}) with respect to their reference values. All the variables evolution is within the bound that corresponds to the fractional requirement reported in Table 2.

The simulated total linear command, including both linear drag-free command and orbit/formation command is showed in Figure 14. The total longitudinal component (x, in red) includes the longitudinal drag compensation that becomes the largest component when the formation transient vanishes. After the transient, the required thrust authority is well below a level of 3 mN. An overall optimization of the control gains may be beneficial in order to improve the transient behavior, as shown from the preliminary simulated results.

Concerning the attitude control design, a simulation representing the attitude control performances in worst-case conditions is represented in Fig. 15, where each satellite is flying in a very low (inclined) orbit under max solar activity. The PSD shows that both pitch and yaw angles meet the requirement bound of Table 2 with margin: concerning the roll angle (not represented in the figure, but details can be found in Ref. 14), a more relaxed

requirement applies, since the laser interferometry measurements can be still performed accepting a larger roll angle, hence not representing a constraint.

VII. Conclusion

The paper presents an overview of NGGM dynamics control system design resulting from the on-going "Consolidation of the system concept for the Next Generation Gravity Mission" study, carried out by TAS-I for ESA. In particular, it shows the major system design challenges arising from the NGGM scientific mission requirements. Indeed, each satellite shall be designed for a long mission lifetime in low orbit, large variation of the solar illumination (due to a non-sun-synchronous orbit), minimum disturbance to the payload and shall be endowed with a complex control system capable of carry out several tasks in close coordination: orbit maintenance, formation keeping, attitude stabilisation, drag compensation and laser beam pointing at micro-radian level.

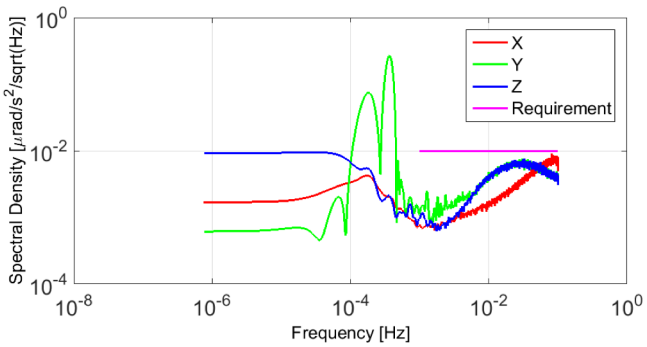

Figure 12. Simulated PSD of the the angular non-gravitational residuals.

The compensation of the along-track drag up to 11 years, turned out to be the main driver of the NGGM system design. The thrust range and modulation capability imposed by the mission, coupled with the challenging lifetime requirement for the thrusters, imply the need both of technological innovations and of dedicated thruster layout and dispatching optimization.

An outline of the AOCS design for NGGM has been presented, in its latest version with the on-going investigations on the open points linked basically to the definition of the mission and operations scenarios. This design is based on a *model-based control design*, specifically on the Embedded Model Control methodology: the mandatory design in terms of disturbance dynamics, their measurement and rejection for the formation and drag-free control has been described.

The design of the orbit and formation control was tackled through the innovative concepts of formation triangle and the formation local orbital frame (FLOF). This led to a new set of CW-type equations, suitable to design a formation control which is capable of controlling in an integrated way distance and altitude. An enhanced multi-rate and multi-hierarchical formation control law architecture was conceived to overcome the possible weaknesses concerning the formation stability in some orbital conditions. Specifically, we envisaged a combination of two different control strategies actuating at very different time units. The secular perturbations, below the orbital period, are tackled by a low-frequency feedback loop leveraging the formation position variables. Then, a further feedback loop was added, involving the formation rate variables and aiming at ensuring their stability.

Extensive simulated results, run via an E2E high-fidelity simulator, proved the validity of the design concept and showed how the control performances meet the mission requirements.

References

[1] Cesare S., Allasio A., Anselmi A., Dionisio S., Mottini S., Parisch M., Massotti L., Silvestrin P., *The European way to gravimetry: From GOCE to NGGM*, *Advances in Space Research*, 18 December 2015, doi: 10.1016/j.asr.2015.12.012

[2] Canuto E., Molano Jimenez A., Bacchetta A., Buonocore M., Cesare S., Girouart B., Massotti L., *The control challenges for the Next Generation Gravity Mission*, *AIAA Guidance, Navigation, and Control Conference 2013*, Boston, Massachusetts, 19-22 August 2013, ISBN: 9781624102240, DOI: 10.2514/6.2013-4639

[3] Bacchetta A., Buonocore M., Cesare, S., Dionisio S., Parisch M., Torasso A., Canuto E., Girouart B., Massotti L., *The Results of the Next Generation Gravity Mission AOCS Study*, *GNC 2014: 9th International ESA Conference on Guidance, Navigation and Control Systems,* Porto, Portugal, 2-6 June 2014

[4] Gruber T., et al., *Temporal aliasing effects on future gravity satellite missions and their assessment - Lessons from the ESA-SC4MGV project*, European Geosciences Union General Assembly 2015

[5] Pail R., et al., *Science and User Needs for Observing Global Mass Transport to Understand Global Change and to Benefit Society*, Surveys in Geophysics, Springer, 2015

[6] *ESA M5 Call - Technical Annex*, ESA-SCI-F-ESTEC-TN-2016-002, April 2016

[7] Canuto E., *Drag-free and attitude control for the GOCE satellite*, Automatica, 44(7) 2008 1766-1780

[8] Canuto E., Montenegro C.P., Colangelo L., Lotufo M. A., *Active Disturbance Rejection Control and Embedded Model Control: A case study comparison*, in Proceedings of the 33rd Chinese Control Conference, 2014

[9] Canuto E., Colangelo L., Buonocore M., Massotti L., Girouart B., *Orbit and formation control for low-earth-orbit gravimetry drag-free satellites,* in Proceedings of the Institution of Mechanical Engineers, Part G: Journal of Aerospace Engineering 229(7) 2014 1194-1213.

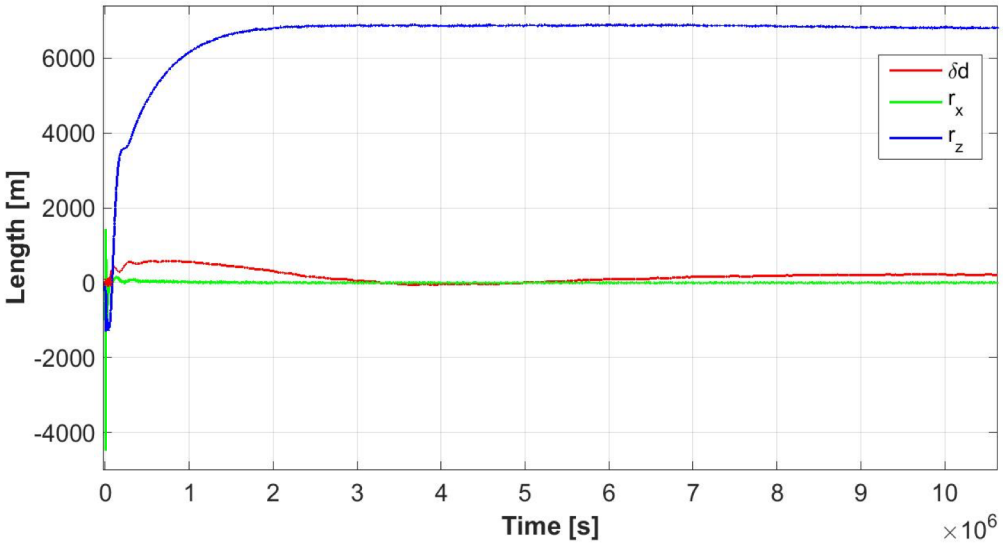

Figure 13. Formation variable perturbations (formation mean tracking errors).

[10] Canuto E., Colangelo L., Lotufo M. A., Dionisio S., *Satellite-to-satellite attitude control of a long-distance spacecraft formation for the Next Generation Gravity Mission*, European Journal of Control, Volume 25, September 2015, Pages 1-16, ISSN 0947-3580.

[11] URL: http://www.esa.int/export/esaLP/goce.html

[12] URL: http://op.gfz-potsdam.de/grace/index_GRACE.html

[13] Canuto E., Colangelo L., *Angular drag-free control and fine satellite-to-satellite pointing for the Next Generation Gravity Missions*, European Control Conference (ECC), 2014

[14] Bacchetta A., Colangelo L., Canuto E., Dionisio S., Massotti L., Novara C., Parish M., Silvestrin P., *From GOCE to NGGM: Automatic Control Breakthroughs for European future Gravity Missions*, in Proc. of the 20th IFAC World Congress, Toulouse, 2017

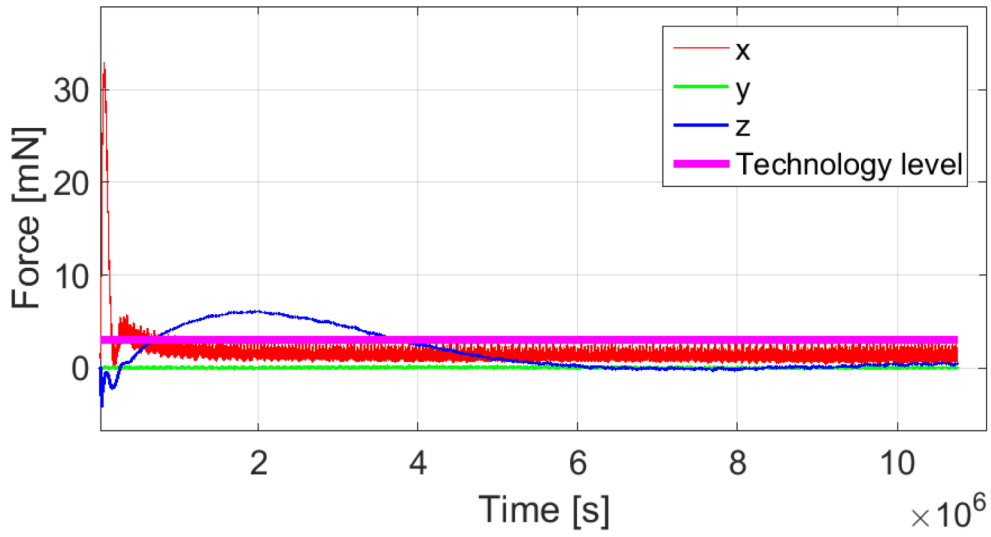

Figure 14. Total linear command. "Technology level" stand for the available thrust authority, limited by the technology available or under development. This limit can be overcome with the use of a larger thruster in the flight direction *x*, scalable from the GOCE thruster class. This issue will be deeply analized in the continuation of the NGGM system study.

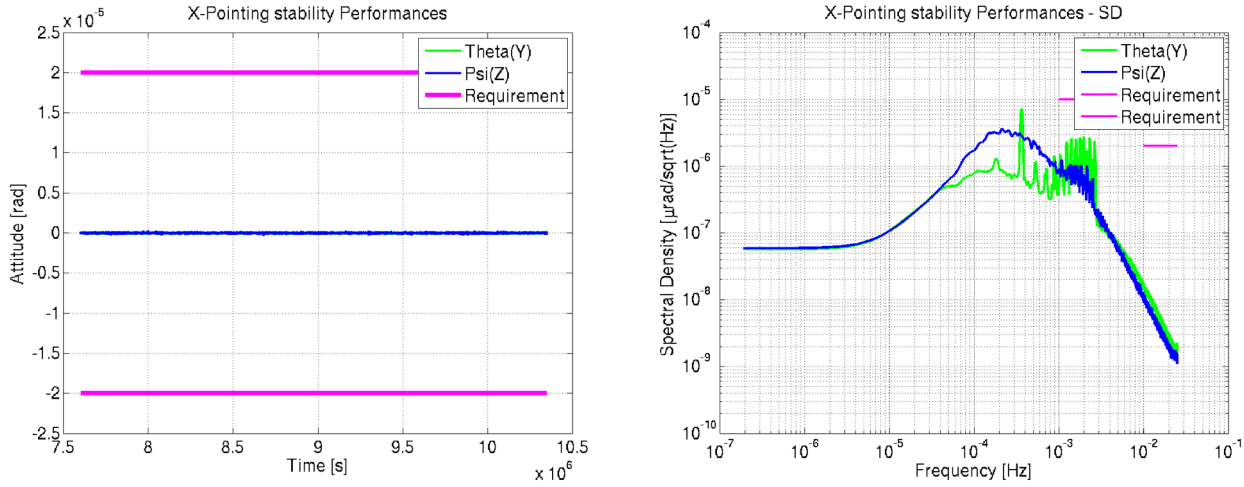

Figure 15. Attitude pointing control performance (inclined pair, max solar activity).